Supporting Information for "A La Niña-like climate response to south African biomass burning aerosol in CESM simulations"

Anahita Amiri-Farahani*[1,2], Robert J. Allen[2], King-Fai Li[1], Pierre Nabat[3],

Daniel M. Westervelt[4]

[1]University of California Riverside, Department of Environmental Sciences, Riverside, CA, USA

[2]University of California Riverside, Department of Earth and Planetary Sciences, Riverside, CA, USA

[3]Centre National de Recherches Météorologiques, UMR3589, Météo-France-CNRS, Toulouse, France

[4]Lamont-Doherty Earth Observatory, Columbia University, Palisades, New York, USA

* Now at Climate and Space Sciences and Engineering, University of Michigan, Ann Arbor, USA

Contents of this file

Semi-empirical fine mode direct radiative effects without dust and sea salt

Aerosol vertical profiles are obtained from the space-borne Cloud Aerosol Lidar with Orthogonal Polarization (CALIOP) (Liu et al., 2009; Winker et al., 2013). CALIOP is able to distinguish between dust and other type of aerosols, which generally do not depolarize light, resulting in six aerosol categories, including dust, marine, smoke, polluted dust, polluted continental, and clean continental (Omar et al., 2009). However, these aerosol categories were not used−the total aerosol vertical distribution was applied regardless of

aerosol type. Daytime CALIPSO Level 2.0 data from June 2006 to October 2011 were processed to obtain a clear-sky aerosol extinction coefficient at 532 nm at the T42 spatial resolution and 500-m vertical resolution of the Monte Carlo Aerosol Cloud Radiation (MACR) model (Podgorny et al., 2000; Choi & Chung, 2014). The data gaps are filled using available neighboring data through linear interpolation. A climatological seasonal cycle for the entire data period is then constructed. The aerosol vertical profile from CALIPSO is scaled to match the AOD observations obtained by integrating AERONET, MODIS, and MISR data (Chung et al., 2016). To adjust the magnitude of AOD over cloud by CALIPSO data, 5°x2° June 2006 to January 2012 globally gridded monthly mean daytime CALIPSO lidar Level 3.0 data (Winker et al., 2013) is used, specifically, the ratio of clear-sky AOD to above-cloud AOD. This is used to modify the aerosol amount over cloud at each grid cell in the MACR model. For coarse-mode aerosols (which are not used here), the same vertical profiles are used. Because coarse-mode aerosols are not very absorbing, the effect on the vertical profile is very small (Choi & Chung, 2014).

The direct aerosol effect is obtained by incorporating the integrated global aerosol data into an updated version of the MACR model(Podgorny et al., 2000; Choi & Chung, 2014). MACR is based on the Monte Carlo Independent Column Approximation (McICA) and uses satellite observations to describe multilayer cloud, surface albedo, and stratospheric column ozone, as well as ERA-Interim Reanalyzes for precipitable water. The 2001-2010 surface albedo and stratosphere column ozone come from the Clouds and the Earth's Radiant Energy System (CERES) Synoptic Radiative Fluxes and Clouds (SYN) monthly product. Clouds come from the 2001-2010 averages of the merged daytime monthly mean CERES ISCCP-D2-like product, which is based on combined geostationary cloud

retrievals and cloud retrievals from Terra/Aqua MODIS (Choi & Chung, 2014). Clouds were combined into four types: low, mid, high, and convective clouds. Between the four types, a random overlap scheme was applied. The key element of this updated version is the Monte Carlo radiative transfer solver combined with the Monte Carlo integration in the multi-dimensional parameter space, including solar zenith angles, aerosol cloud configurations, and spectral bands. Despite monthly resolution of the three-dimensional model inputs, MACR was run for all 365 days of the year to address variations in the solar zenith angle, declination, and eccentricity of Earth's orbit. For each day, 40,000 photons were deployed, and monthly inputs were interpolated in time and the model output was averaged over each month. The benefits of the Monte Carlo approach for radiative transfer is that it provides more accurate flux values relative to two stream approximations for both clear and cloudy skies (Barker et al., 2003).

Our aerosol direct radiative effect is subject to several sources of uncertainty. AERONET single-scatterng albedo (SSA), in particular, is subject to uncertainties due to various assumptions used in the retrieval algorithms. Climatological AERONET SSA differs from in situ measured SSA by up to 0.02, with underestimation in low Angstrom exponent areas and overestimation in high Angstrom exponent areas (Eck et al., 2010). The maximum error of AERONET AOD is between 0.01 and 0.015 for Level 2.0 data (Eck et al., 1999). A direct validation of AERONET absorption AOD (AAOD) with unmanned aerial vehicle observations shows that AERONET AAOD errors are less than 20% (Corrigan et al., 2008).

Sensitivity tests were performed to quantify the uncertainty (primarily due to AOD and SSA) in the observationally constrained fine-mode aerosol direct radiative effect used here

(Chung et al., 2016). Fine-mode aerosols yield atmospheric absorption of 3.88 W m^{-2}. This varies from 3.63 W m^{-2} (least absorbing case) to 4.08 W m^{-2} (most absorbing case), yielding an uncertainty range of about $\pm$0.25 W m^{-2}. These uncertainty estimates are based on modifying BC AOD and BC/organic aerosol (OA) SSA. Three different sets of simulated SSA are used:

SSA1=(0.19xBC AOD+0.85xOA AOD+sulfate AOD+seasalt AOD+0.96xdust AOD)/total AOD;

SSA2=(0.14xBC AOD+0.80xOA AOD+sulfate AOD+seasalt AOD+0.96xdust AOD)/total AOD; and

SSA3=(0.19xBC AOD+0.98xOA AOD+sulfate AOD+seasalt AOD+0.96xdust AOD)/total AOD.

BC AOD above refers to the GOCART BC AOD at 550 nm (and similarly for the other aerosol species). Parameters (e.g., 0.19 for BC SSA) in the above equations come from observational studies (Magi, 2009, 2011). In addition, in SSA2 (more absorbing case), the magnitude of BC AOD was doubled, given that simulated BC may be significantly underestimated (Bond et al., 2013). These are then nudged toward the AERONET SSA, giving three sets of semi-observational SSA (Chung et al., 2016). In terms of fine-mode dust and sea salt, with a baseline atmospheric heating estimate is 0.23 W m^{-2}, sensitivity tests yield a corresponding uncertainty range from 0.16 to 0.26 W m^{-2}. These sensitivity tests are based on using GOCART versus GISS ModelE2 fine-mode dust and sea salt (Chung et al., 2016).

Uncertainty in the absorbing aerosol profile as derived from CALIPSO also exists, including attenuation of the lidar signal. For example, optically thick aerosol layers above African biomass burning can completely attenuate the signal, leading to no retrievals below these levels (Das et al., 2017). Although our observationally constrained aerosol

vertical profile is not based on individual CALIPSO aerosol categories, such attenuation can also lead to misclassification of aerosol type by the classification algorithm (Burton et al., 2013; Kacenelenbogen et al., 2014). However, our use of CALIPSO's total aerosol vertical distribution, regardless of aerosol type, also leads to additional uncertainty in the absorbing aerosol vertical profile. This uncertainty is much smaller than the overall differences between the CALIPSO profile and simulated BC profiles

References

Barker, H. W., Stephens, G. L., Partain, P. T., Bergman, J. W., Bonnel, B., Campana, K., ... Yang, F. (2003). Assessing 1d atmospheric solar radiative transfer models: Interpretation and handling of unresolved clouds. *J. Climate*, *16*, 2676-2699, doi: 10.1175/1520-0442(2003)016¡2676:ADASRT¿2.0.CO;2.

Bond, T. C., Doherty, S. J., Hahey, D. W., & et al. (2013). Bounding the role of black carbon in the climate system: A scientific assessment. *J. Geophys. Res.*, *118*, 5380-5552, doi:10.1002/jgrd.50171.

Burton, S. P., Ferrare, R. A., Vaughan, M. A., Omar, A. H., Rogers, R. R., Hostetler, C. A., & Hair, J. W. (2013). Aerosol classification from airborne HSRL and comparisons with the CALIPSO vertical feature mask. *Atmospheric Measurement Techniques*, *6*, 1397-1412, doi: 10.5194/amt-6-1397-2013.

Choi, J.-O., & Chung, C. E. (2014). Sensitivity of aerosol direct radiative forcing to aerosol vertical profile. *Tellus B*, *66*, 24376, doi: 10.3402/tellusb.v66.24376,.

Chung, C. E., Chu, J.-E., Lee, Y., van Noije, T., Jeoung, H., Ha, K.-J., & Marks, M. (2016). Global fine-mode aerosol radiative effect, as constrained by comprehensive observations. *Atmospheric Chemistry and Physics*, *16*(13), 8071-8080, 10.5194/acp-16-8071-2016.

Corrigan, C. E., Roberts, G. C., Ramana, M. V., Kim, D., & Ramanathan, V. (2008). Capturing vertical profiles of aerosols and black carbon over the Indian Ocean using autonomous unmanned aerial vehicles. *Atmos. Chem. Phys.*, *8*, 727-747, doi: 0.5194/acp-8-737-2008.

Das, S., Harshvardhan, H., Bian, H., Chin, M., Curci, G., Protonotariou, A. P., ...

Liu, X. (2017). Biomass burning aerosol transport and vertical distribution over the South African-Atlantic region. *J. Geophys. Res.-Atmos.*, *22*, 6391-6415, doi: 10.1002/2016JD026421.

Eck, T. F., Holben, B. N., Reid, . S., Dubovik, O., Smirnov, A., O'Neill, N. T., ... Kinne, S. (1999). Wavelength dependence of the optical depth of biomass burning, urban, and desert dust aerosols. *J. Geophys. Res.-Atmos.*, *104*, 31,333-31,349, doi: 10.1029/1999JD900923.

Eck, T. F., Holben, B. N., Sinyuk, A., Pinker, R. T., Goloub, P., Chen, H., ... Xia, X. (2010). Climatological aspects of the optical properties of fine/coarse mode aerosol mixtures. *J. Geophys. Res.-Atmos.*, *115*, D19205, doi: 10.1029/2010JD014002.

Kacenelenbogen, M., Redemann, J., Vaughan, M. A., Omar, A. H., Russell, P. B., Burton, S., ... Hostetler, C. A. (2014). An evaluation of CALIOP/CALIPSO's aerosolabovecloud detection and retrieval capability over North America. *J. Geophys. Res.-Atmos.*, *119*, 230-244, doi: 10.1002/2013JD020178.

Liu, Z., Vaughan, M., Winker, D., Kittaka, C., Getzewich, B., Kuehn, R., ... Hostetler, C. (2009). The CALIPSO Lidar Cloud and Aerosol Discrimination: Version 2 Algorithm and Initial Assessment of Performance. *Journal of Atmospheric and Oceanic Technology*, *26*(7), 1198-1213, 10.1175/2009JTECHA1229.1.

Magi, B. I. (2009). Chemical apportionment of southern african aerosol mass and optical depth. *Atmos. Chem. Phys.*, *9*, 7643-7655, doi: 10.5194/acp-9-7643-2009.

Magi, B. I. (2011). Corrigendum to "Chemical apportionment of southern African aerosol mass and optical depth" . *Atmos. Chem. Phys.*, *11*, 4777-4778, doi: 10.5194/acp-11-4777-2011.

Omar, A. H., Winker, D. M., Vaughan, M. A., Hu, Y., Trepte, C. R., Ferrare, R. A., ... Liu, Z. (2009). The CALIPSO automated aerosol classification and lidar ratio selection algorithm. *Journal of Atmospheric and Oceanic Technology*, *26*, 1994-2014, doi: 10.1175/2009JTECHA1231.1.

Podgorny, I. A., Conant, W. C., Ramanathan, V., & Satheesh, S. K. (2000). Aerosol modulation of atmospheric and solar heating over the tropical Indian Ocean. *Tellus, Ser. B*, *52*, 947-958, doi: 10.3402/tellusb.v52i3.17077.

Winker, D. M., Tackett, J. L., Getzewich, B. J., Liu, Z., Vaughan, M. A., & Rogers, R. R. (2013). The global 3-D distribution of tropospheric aerosols as characterized by CALIOP. *Atmospheric Chemistry and Physics*, *13*(6), 3345–3361, 10.5194/acp-13-3345-2013.

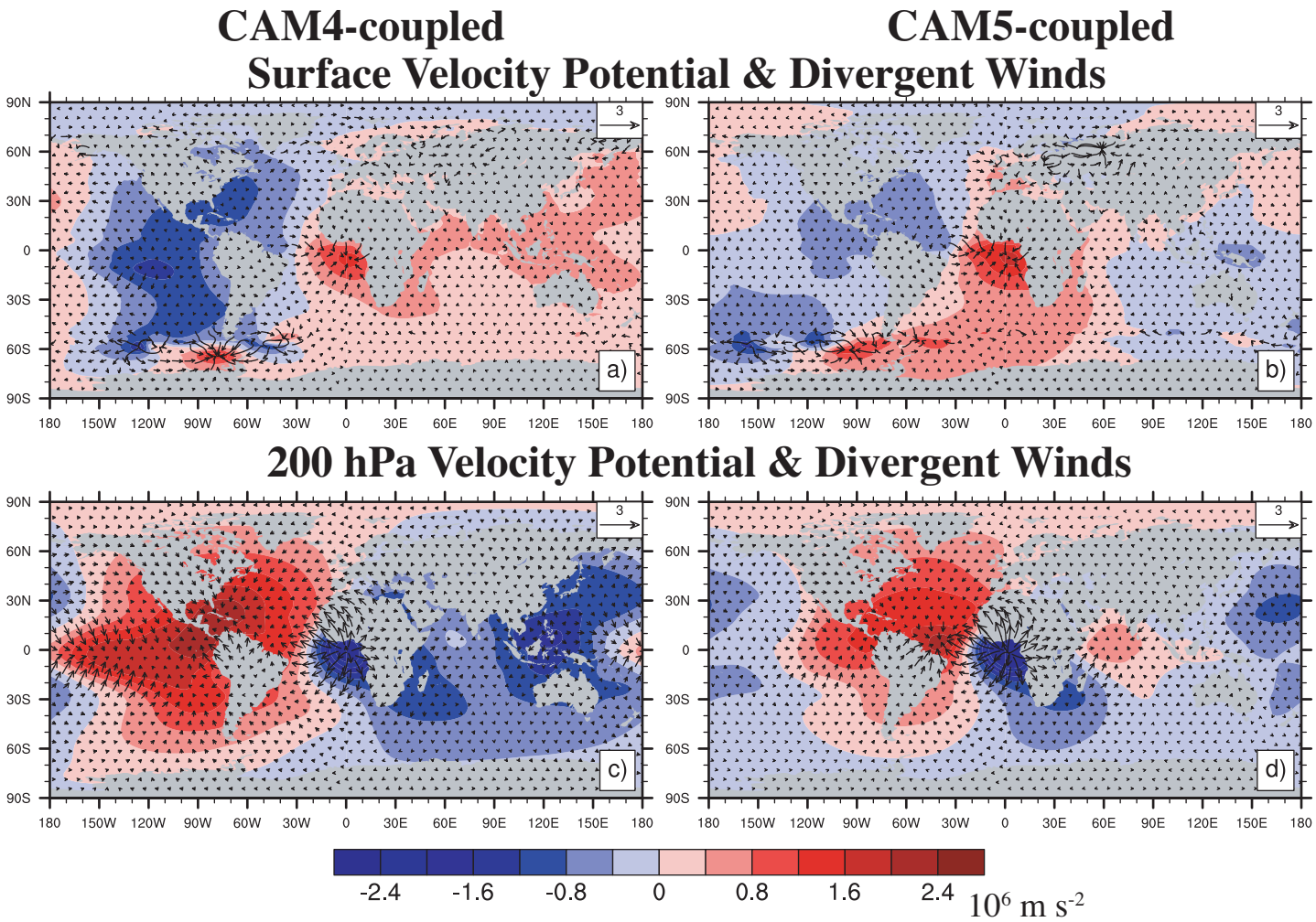

Figure S1. Annual mean velocity potential and divergent wind response at (top panels) the surface and (bottom panels) 200 hPa for (left panels) CAM4-coupled and (right panels) CAM5-coupled. These experiments show the climate response to global semi-empirical fine-mode aerosol direct radiative effect using coupled ocean-atmosphere simulations. Velocity potential and divergent wind units are 10^6 m s^{-2} and m s^{-1}, respectively.

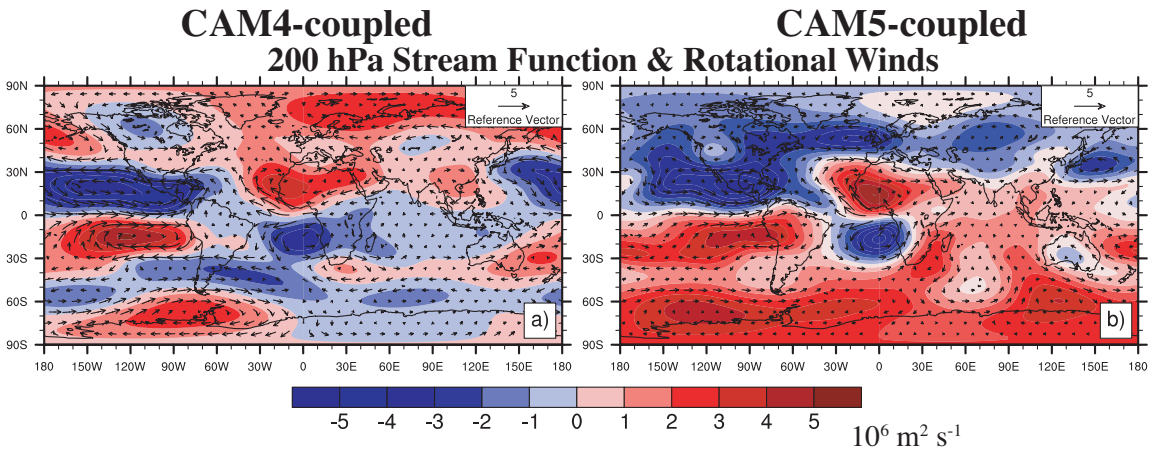

Figure S2. Annual mean 200 hPa stream function and rotational wind response for (a) CAM4-coupled and (b) CAM5-coupled. These experiments show the climate response to global semi-empirical fine-mode aerosol direct radiative effect using coupled ocean-atmosphere simulations. Units are 10^6 m^2 s^{-1}. Vectors show the rotational component of the wind, with units of m s^{-1}.

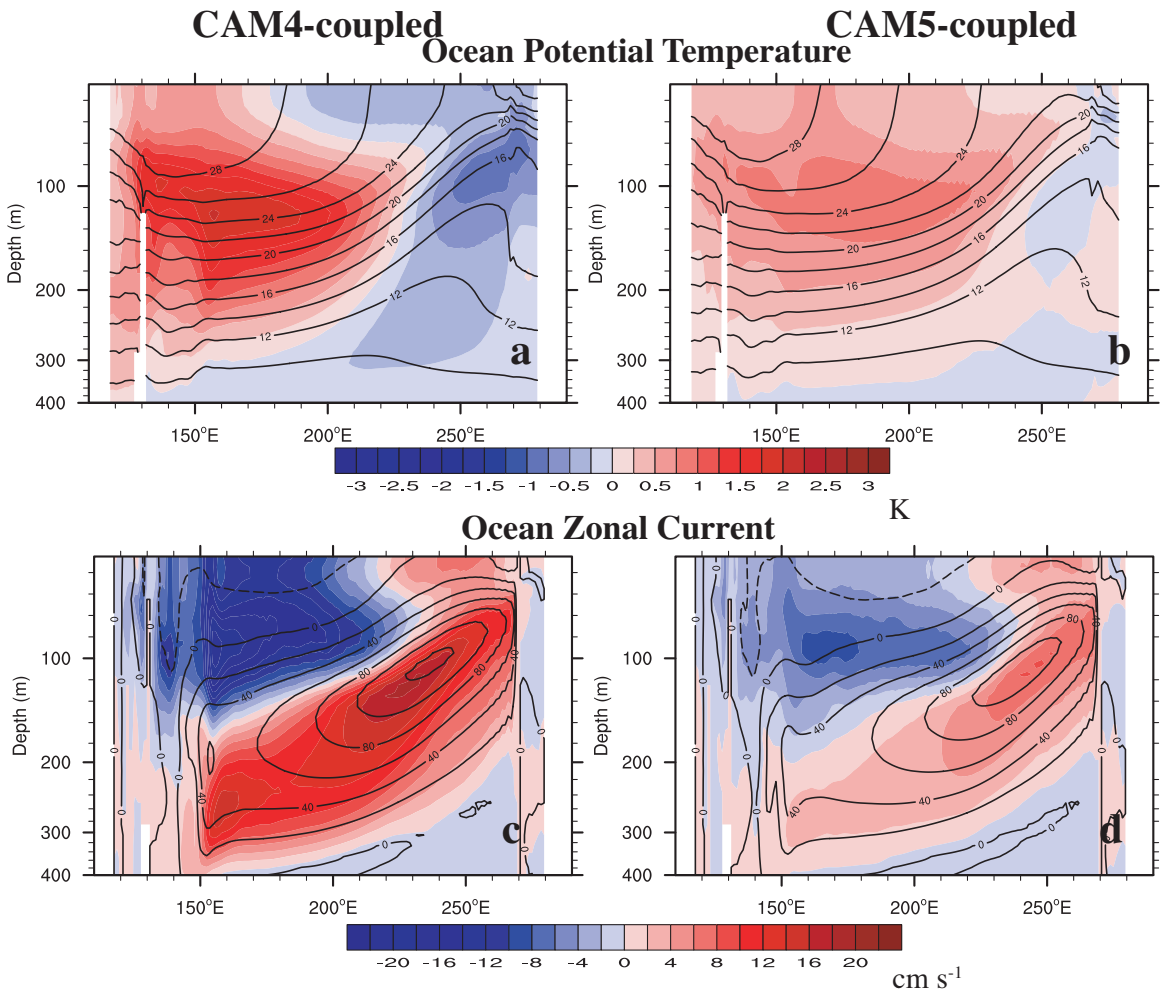

Figure S3. Annual mean equatorial cross section of oceanic (top panels) potential temperature and (bottom panels) zonal current response over the Pacific Ocean for (left panels) CAM4-coupled and (right panels) CAM5-coupled. These experiments show the climate response to global semi-empirical fine-mode aerosol direct radiative effect using coupled ocean-atmosphere simulations. Also included as black contours are the corresponding climatologies. Units are K and cm s^{-1}, respectively.

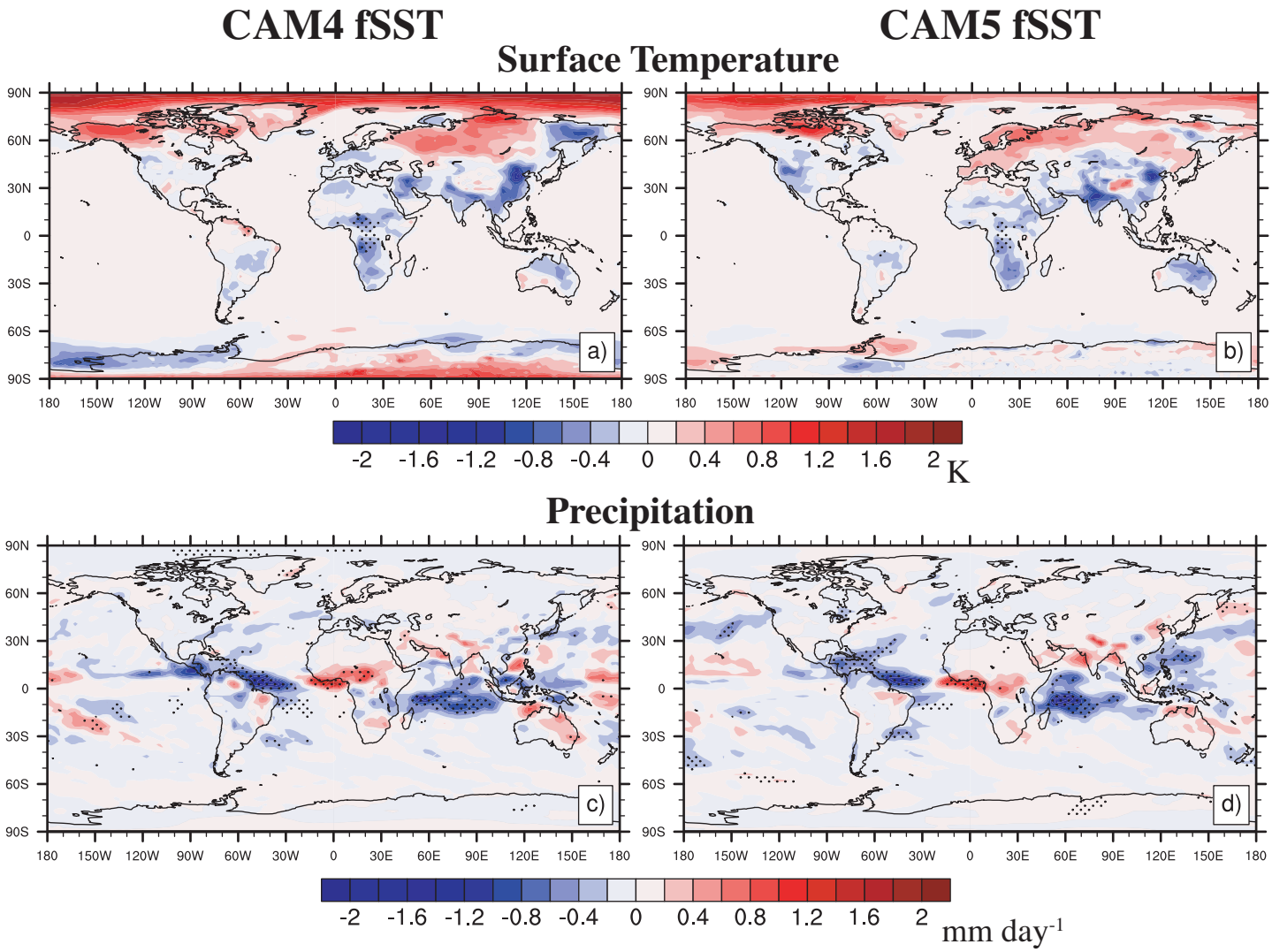

Figure S4. Annual mean (a,b) surface temperature and (c,d) precipitation response for (left panels) CAM4-fSST and (right panels) CAM5-fSST. These experiments show the fast-response to global semi-empirical fine-mode aerosol direct radiative effect using fixed SSTs. Symbols denote significance at 90% confidence level, based on a t-test for the difference of means using the pooled variance. Temperature and precipitation units are K and mm day^{-1}, respectively. The global annual mean change in surface temperature is 0.000074 K for CAM4-fSST and 0.0065 K for CAM5-fSST (not significant at the 90% confidence level). The corresponding global annual mean change in precipitation is -0.045 and -0.043 mm day^{-1}, respectively (both significant at the 99% confidence level).

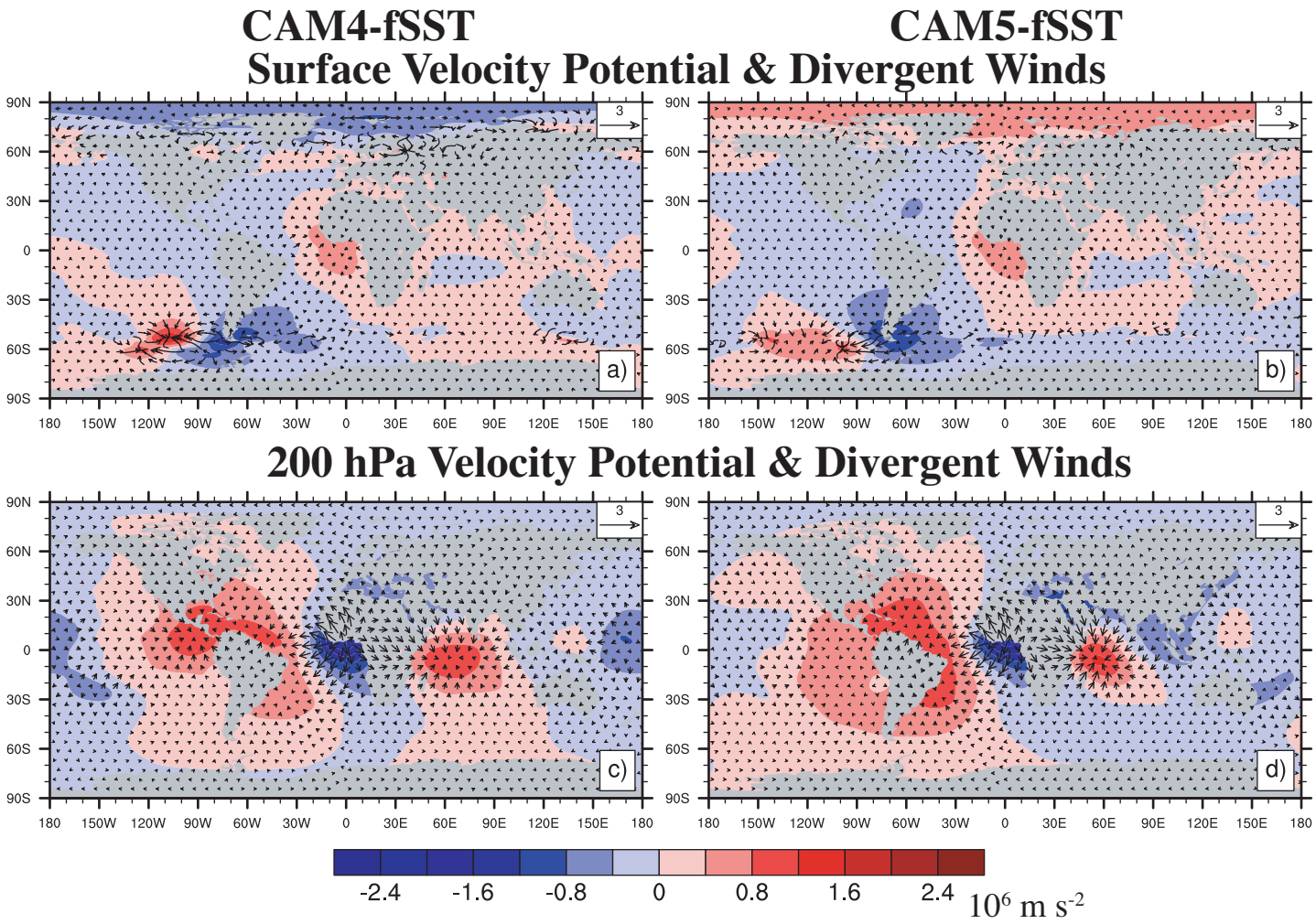

Figure S5. Annual mean velocity potential and divergent wind response at (top panels) the surface and (bottom panels) 200 hPa for (left panels) CAM4-fSST and (right panels) CAM5-fSST. These experiments show the fast-response to global semi-empirical fine-mode aerosol direct radiative effect using fixed SSTs. Velocity potential and divergent wind units are 10^6 m s^{-2} and m s^{-1}, respectively.

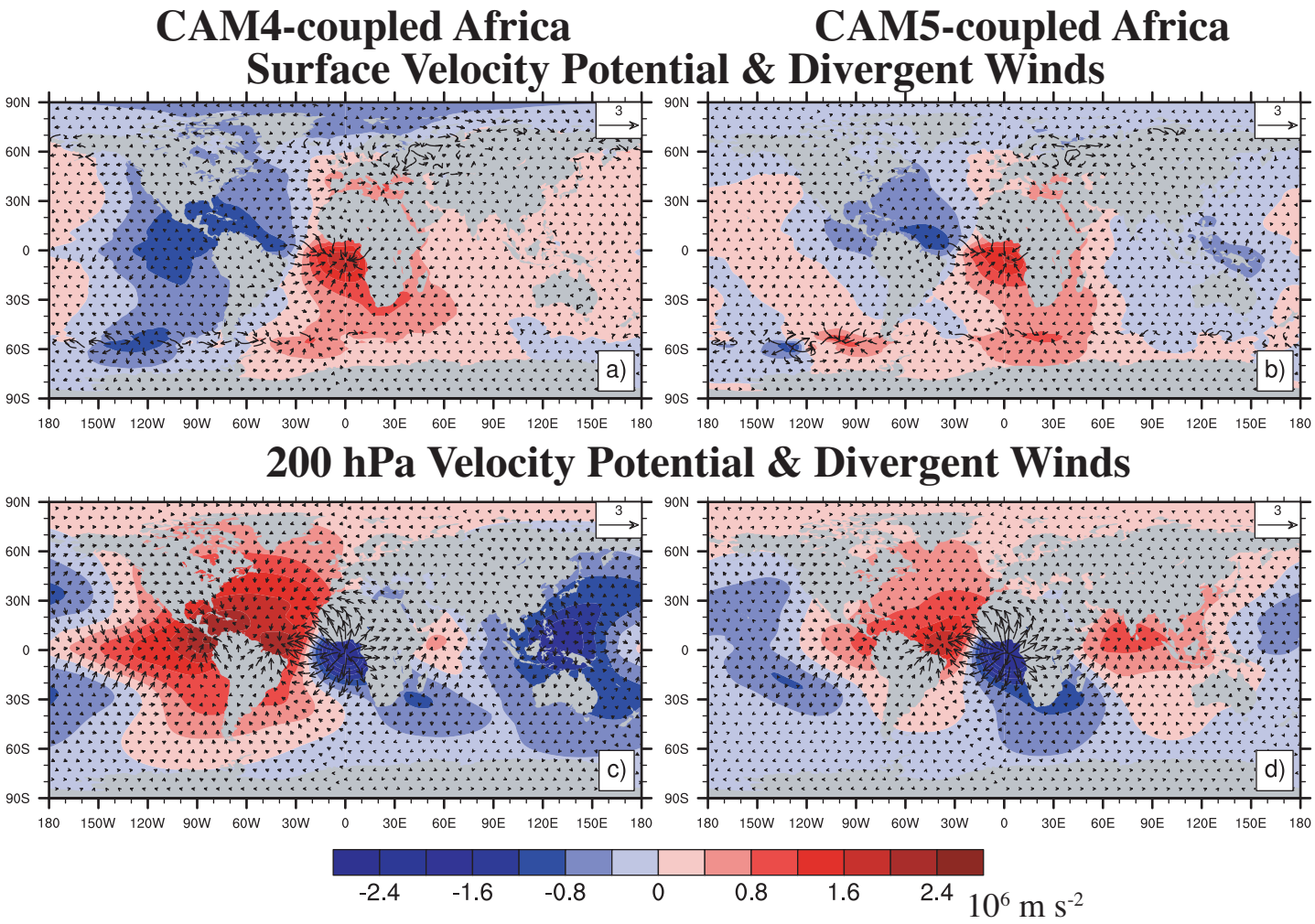

Figure S6. Annual mean velocity potential and divergent wind response at (top panels) the surface and (bottom panels) 200 hPa for (left panels) CAM4-coupled Africa and (right panels) CAM5-coupled Africa. These experiments show the climate response to semi-empirical fine-mode aerosol direct radiative effect without dust and sea salt over Africa only using coupled ocean-atmosphere simulations. Velocity potential and divergent wind units are 10^6 m s^{-2} and m s^{-1}, respectively.

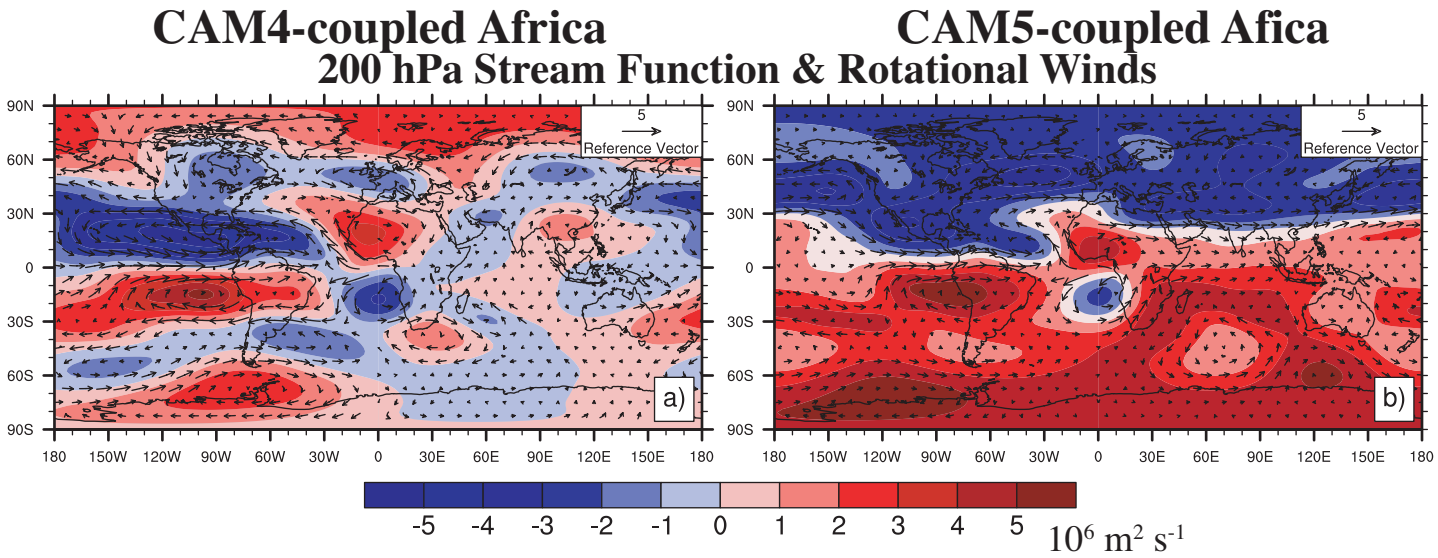

Figure S7. Annual mean 200 hPa stream function and rotational wind response for (a) CAM4-coupled Africa and (b) CAM5-coupled Africa. These experiments show the climate response to semi-empirical fine-mode aerosol direct radiative effect without dust and sea salt over Africa only using coupled ocean-atmosphere simulations. Units are 10^6 m^2 s^{-1}. Vectors show the rotational component of the wind, with units of m s^{-1}.

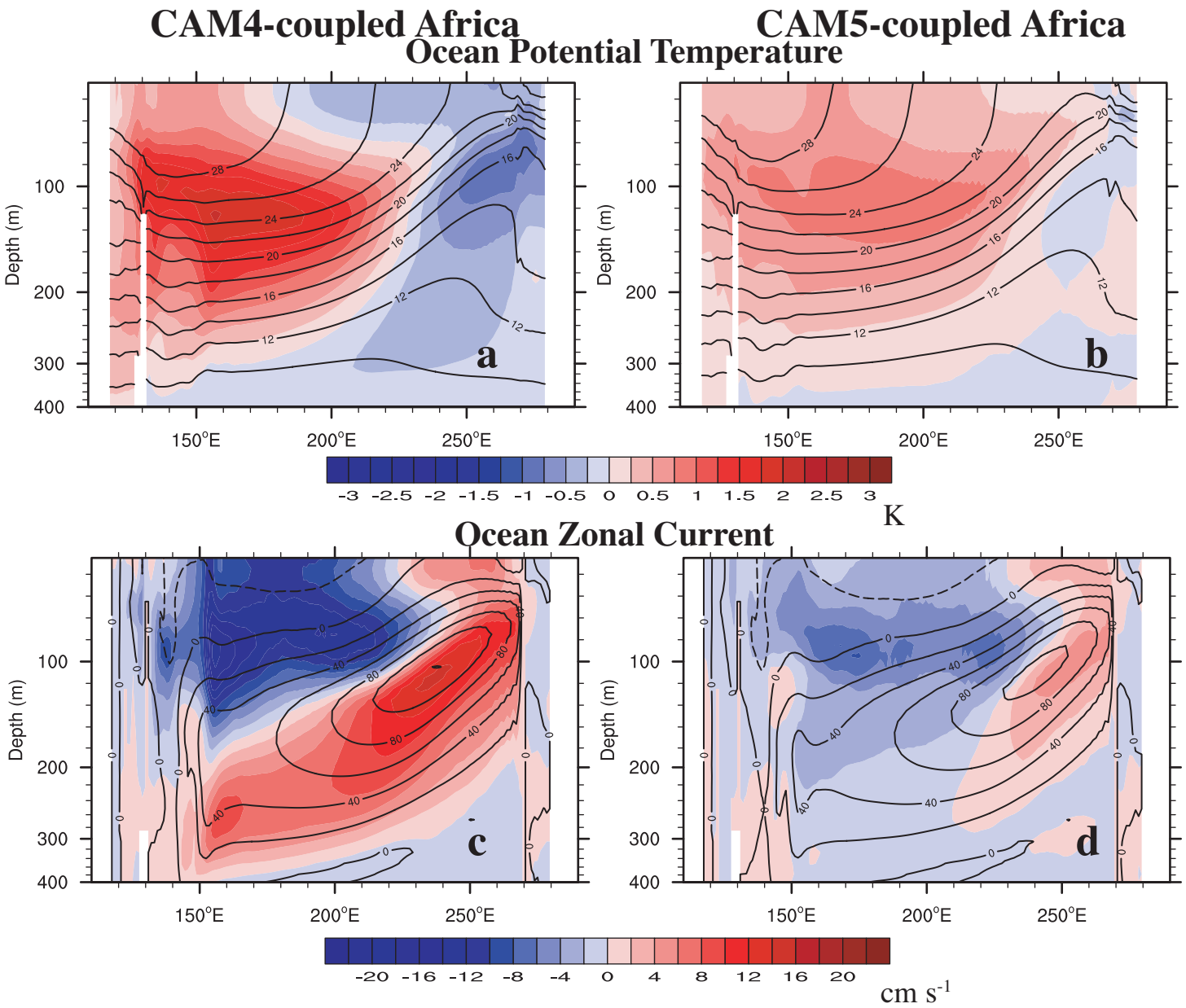

Figure S8. Annual mean equatorial cross section of oceanic (top panels) potential temperature and (bottom panels) zonal current response over the Pacific Ocean for (left panels) CAM4-coupled Africa and (right panels) CAM5-coupled Africa. These experiments show the climate response to semi-empirical fine-mode aerosol direct radiative effect without dust and sea salt over Africa only using coupled ocean-atmosphere simulations. Also included as black contours are the corresponding climatologies. Units are K and cm s^{-1}, respectively.

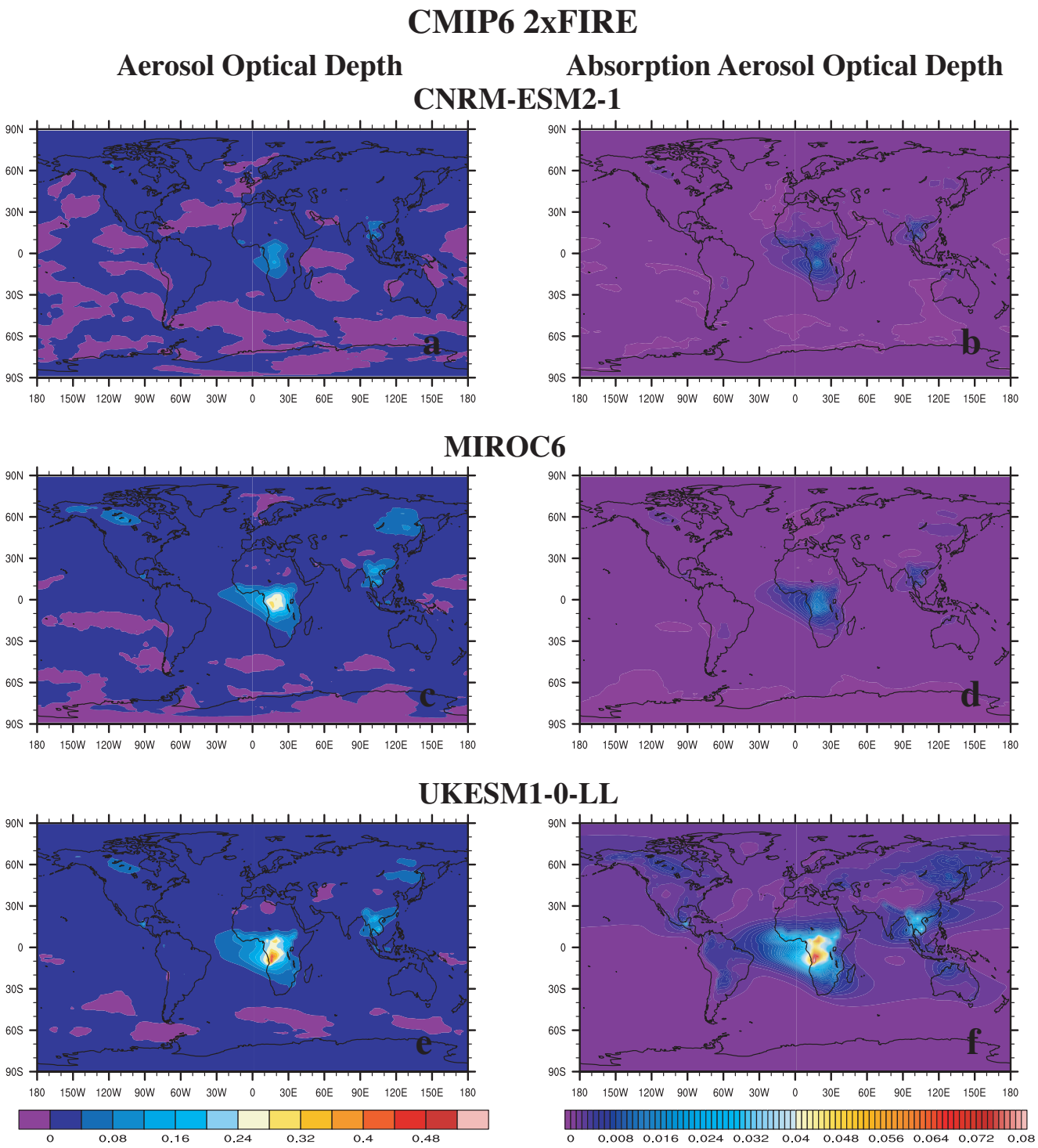

Figure S9. CMIP6 2xFIRE annual mean (left panels) aerosol optical depth (AOD) and (right panels) absorption aerosol optical depth (AAOD) responses for (top panels) CNRM-ESM2-1, (middle panels) MIROC6, and (bottom panels) UKESM1-0-LL. Units are dimensionless.

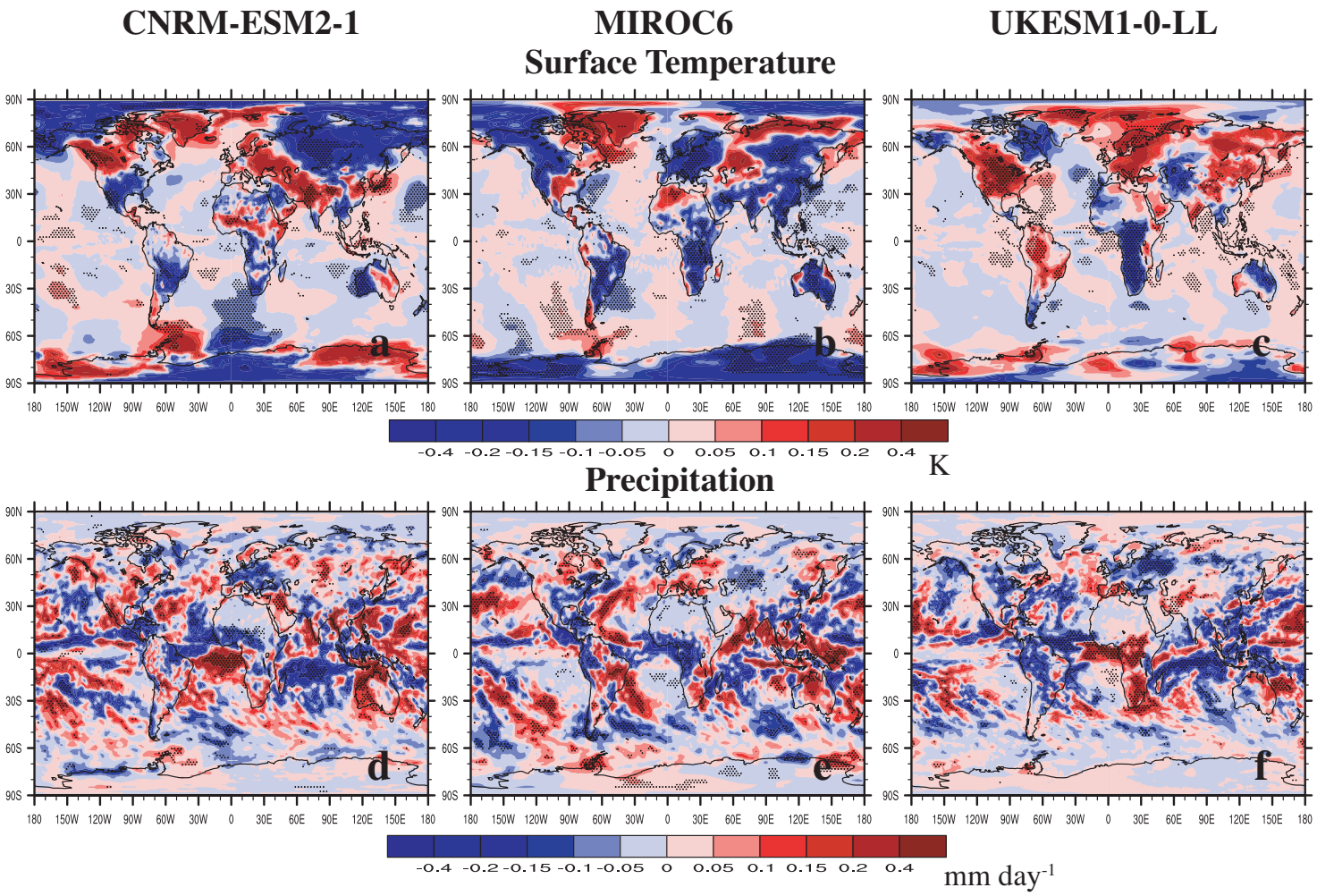

Figure S10. CMIP6 2xFIRE annual mean (a-c) surface temperature and (d-f) precipitation response for (left panels) CNRM-ESM2-1; (center panels) MIROC6; and (right panels) UKESM1-0-LL. Symbols denote significance at 90% confidence level, based on a *t*-test for the difference of means using the pooled variance. Temperature and precipitation units are K and mm day^{-1}, respectively.

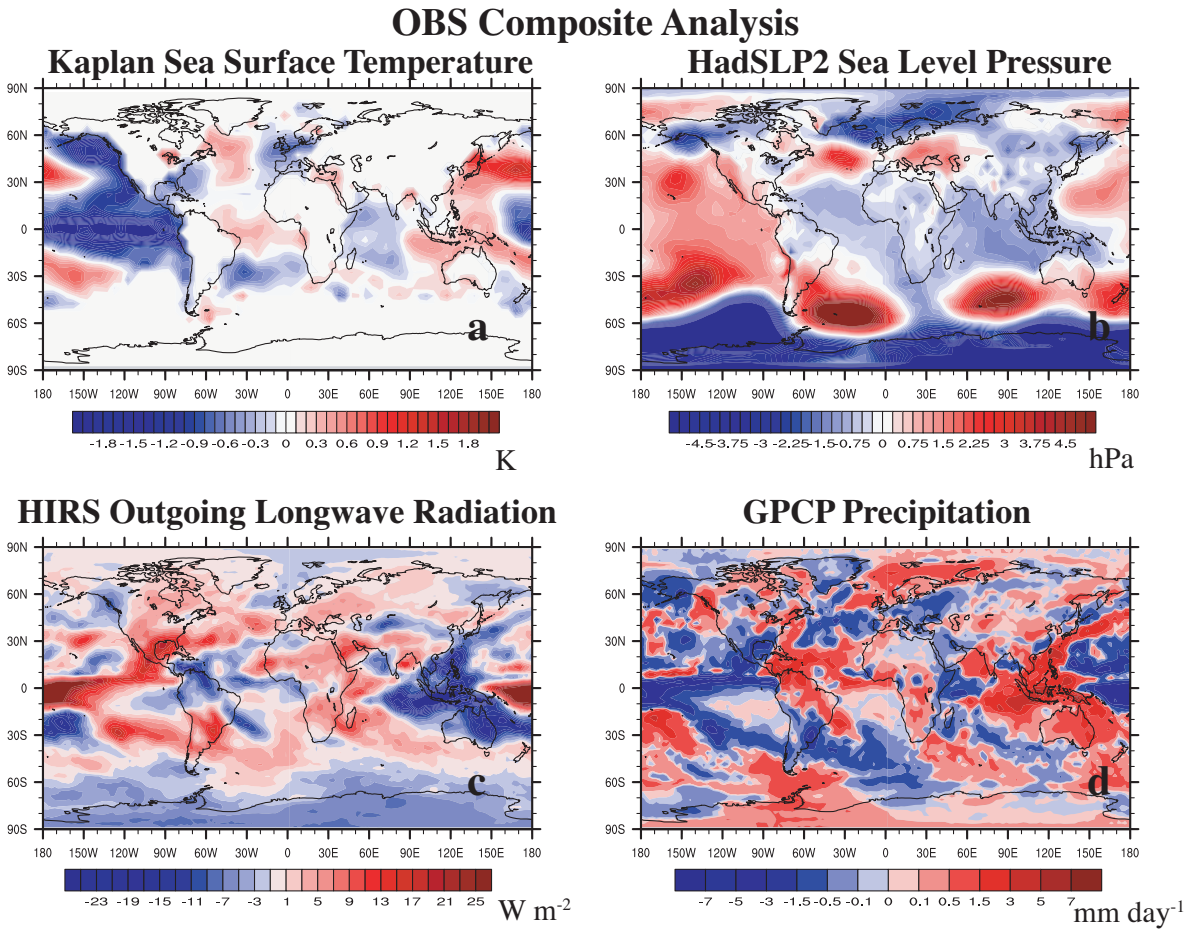

Figure S11. Observation-based September-October-November (SON) composite analysis (high minus low fire years) of dynamical responses including (a) Kaplan sea surface temperature, (b) Hadley Centre sea level pressure (SLP); (c) HIRS outgoing longwave radiation (OLR); and (d) GPCP precipitation. Analysis is based on 1997-2018 SON GFED4s south African biomass burning emissions. Sea surface temperature, SLP, OLR and precipitation units are K, hPa, W m^{-2}, and mm day^{-1}, respectively.